Supporting Information for

Advance in tuning "$d_{33} \propto 1/T_d$" bottleneck: Realizing large d_{33} and high T_d in $Bi_{0.5}Na_{0.5}TiO_3$-based relaxor ferroelectrics

Jie Yin[1], Hong Tao[1], Yuxing Zhang[1], Jihui Han[1], Gang Liu[1], Zhitao Li[2], Xingmin Zhang[3] and Jiagang Wu[1,*]

[1]*Department of Materials Science, Sichuan University, 610064, Chengdu, P. R. China*
[2]*School of Materials Science and Engineering, Tsinghua University, 100084, Beijing, P. R. China*
[3]*Shanghai Synchrotron Radiation Facility, Shanghai Institute of Applied Physics, Chinese Academy of Sciences, Pudong New Area, Shanghai 201204, P. R. China*

*Corresponding author: wujiagang0208@163.com and msewujg@scu.edu.cn

1. Materials selection

To select the critical composition for the further quenching treatment, the relationship between chemical composition and corresponding piezoelectric (d_{33}, k_p) and dielectric (ε_r, tan δ) signals of (1-x-y)$Bi_{0.5}Na_{0.5}TiO_3$-$xBaTiO_3$-$yBi_{0.5}Li_{0.5}TiO_3$ materials are studied, as displayed in Figure S1. Both of the piezoelectric strain constant d_{33} and the electromechanical coupling factor k_p first increase and then decrease with the increasing x and y contents, and d_{33} reaches to the peak value of 253±5 pC/N for x/y=0.055/0.10 [Figures S1a and S1b]. Similar tendency can be observed for the dielectric signals, and the dielectric maximum can be observed in the sample with x/y=0.055/0.10 [Figures S1c and S1d]. Note here that the dielectric responses will increase with the further increment of $Bi_{0.5}Li_{0.5}TiO_3$ content (y≥0.125), but the piezoelectric responses exhibit the inverse trend. Therefore, from a series of $BaTiO_3$- and $Bi_{0.5}Li_{0.5}TiO_3$-doped $Bi_{0.5}Na_{0.5}TiO_3$ compositions, we select $0.845Bi_{0.5}Na_{0.5}TiO_3$-$0.055BaTiO_3$-$0.10Bi_{0.5}Li_{0.5}TiO_3$ as the critical studied composition, because of its superior piezoelectric responses (d_{33}=253±5 pC/N and k_p=0.383).

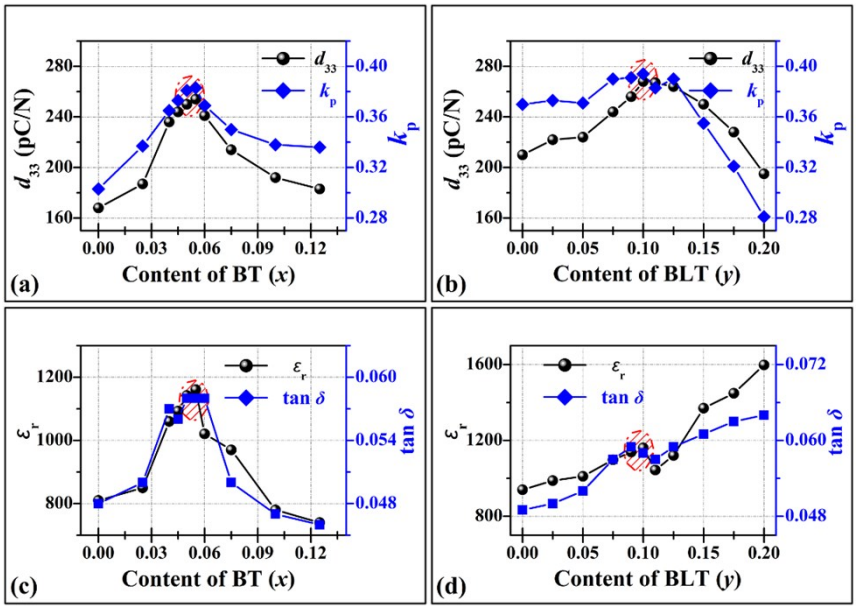

Figure S1. Composition dependence of piezoelectric signals (d_{33}, k_p) and dielectric signals (ε_r, tan δ measured at 1 kHz) of the ceramics with different BT (x)and BLT (y) contents. The red marks highlight the selected composition utilized to experience the quenching treatment.

2. Quenching simulation

The bulk free energy density is expected by Landau theory as:

$$f_{bulk}=\alpha_1(P_x^2+P_y^2+P_z^2)+\alpha_{11}(P_x^4+P_y^4+P_z^4)+\alpha_{12}(P_x^2P_y^2+P_y^2P_z^2+P_z^2P_x^2)+\alpha_{111}(P_x^6+P_y^6+P_z^6)+\alpha_{112}[P_x^4(P_y^2+P_z^2)+P_y^4(P_x^2+P_z^2)+P_z^4(P_x^2+P_y^2)]+\alpha_{123}P_x^2P_y^2P_z^2$$

where α_1, α_{11}, α_{12}, α_{111}, α_{112} and α_{123} are Landau energy coefficients. Note here that the free-energy profile is just a schematic model utilized to illustrate the transition process from the high-temperature cubic phase to the low-temperature ferroelectric phase, and these coefficients are derived from open literatures. [1] To provide a more intuitive display about this temperature-dependent process, we give the profile of free energy against two-dimensional spontaneous polarization P_x and P_y, as provided in Figs. Sn.

Metropolis rule is introduced to our quenching simulation. For the ferroelectric materials system, this rule indicates that the higher the temperature, the greater the probability of jumping over the energy barrier Δf during the cooling process.

$$p=\begin{cases}1, & \text{if } f(p_{new})<f(p_{old})\\ \exp\left(-\dfrac{f(pnew)-f(pold)}{akT}\right), & \text{if } f(p_{new})\geq f(p_{old})\end{cases}$$

where $\Delta f = f(p_{new}) - f(p_{old})$ denotes the variation of the bulk free energy density at a certain temperature T, and k is the Boltzmann constant and a is the tuning parameter.

The initial parameters include:

(1) The initial temperature T_0 = 1100 ℃;

(2) The attenuation function is adopted according to the α = 5℃/min cooling rate of our furnace, that is, the iterative temperature $T_{i+1} = T_0 - \alpha T_i$.

(3) The terminational temperature T_t = 0 ℃;

(4) The length of the Markov chain L_k = 200, and the total number of iterations is 500.

3. Other detailed results

3.1 Dielectric and piezoelectric information

Figure S2 provides the dielectric and piezoelectric information of the samples with six different treatments, and $T_{f\text{-}r}$ is derived from the temperature corresponding to the peak of the temperature-dependent loss tangent marked in **Figure** S2c. Accompanied with the rising $T_{f\text{-}r}$, the relative permittivity ε_r and loss tangent tan δ exhibit a slight decrease and the discrepancy of dielectric responses among different frequencies gradually decrease, as the frequency-dependent dielectric responses shown in **Figure** S2a. The excellent piezoelectricity can be kept to a high temperature for the samples treated with quenching routes, as the *ex-situ* thermal annealing results provided in **Figure** S2b. Temperature-dependent relative dielectric permittivity (ε_r) and loss tangent (tan δ) of the samples treated by six different routes indicate that $T_{f\text{-}r}$ can be greatly increased to a higher temperature region, as shown in **Figure** S2c.

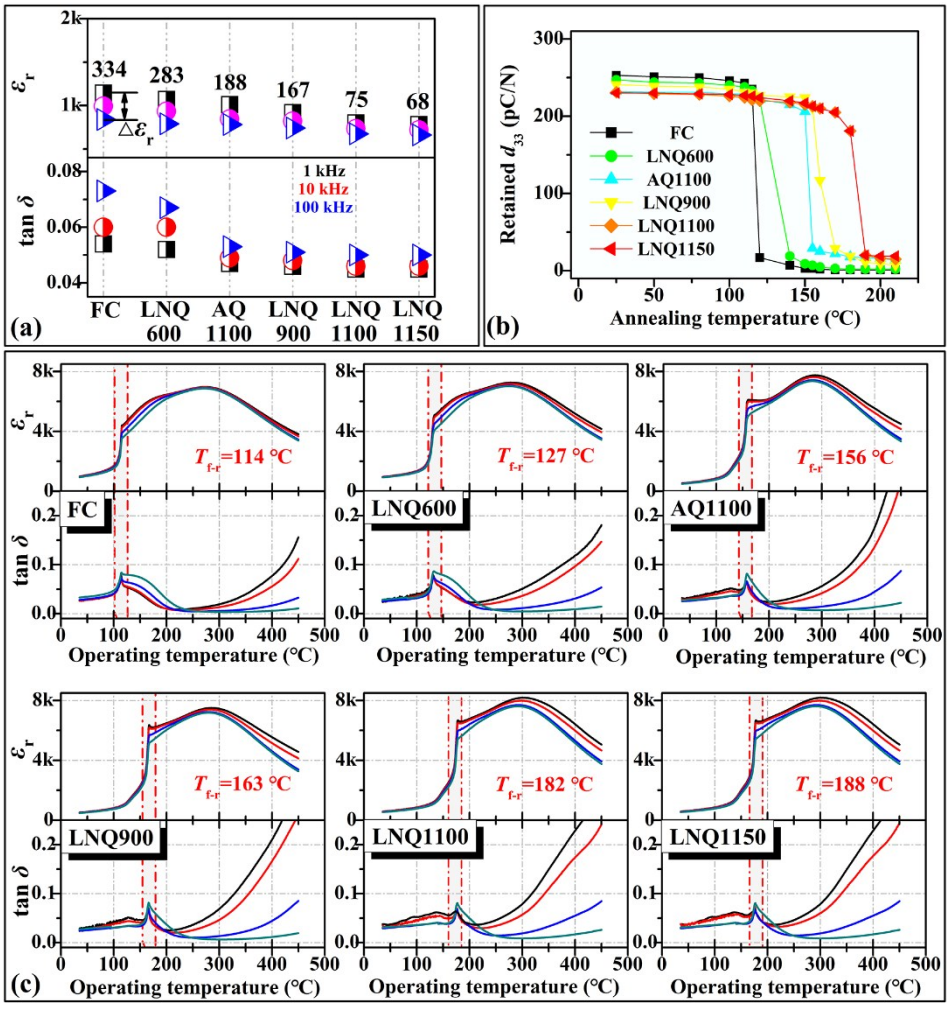

Figure S2. (a) The frequency-dependent (1 kHz, 10 kHz and 100 kHz) variations of relative permittivity ε_r and loss tangent tan δ derived from the samples treated with six

different routes (FC, LNQ600, AQ1100, LNQ900, LNQ1100 and LNQ1150). (b) Temperature-dependent variations of the small signal piezoelectric strain coefficient d_{33} measured in an *ex-situ* way. (c) Temperature-dependent relative dielectric permittivity (ε_r) and loss tangent (tan δ) of the samples treated by six different routes, and the frequency of 100, 1k, 10k and 100kHz were used to detect the dielectric signal.

Figure S3 provide the dielectric and piezoelectric information of the LNQ1100 samples treated with different thermal annealing temperatures in nitrogen atmosphere, and $T_{f\text{-}r}$ is derived from the temperature corresponding to the peak of the temperature-dependent loss tangent marked in **Figure** S3a. Temperature-dependent relative dielectric permittivity (ε_r) and loss tangent (tan δ) of the LNQ1100 samples treated with different annealing routes indicate that $T_{f\text{-}r}$ is decreased to a lower temperature, as shown in **Figure** S3a. Accompanied with the decreasing $T_{f\text{-}r}$, the relative permittivity ε_r and loss tangent tan δ exhibit a slight increase and the discrepancy of dielectric responses among different frequencies gradually increase, as the frequency-dependent dielectric responses shown in **Figure** S3b. The piezoelectricity can only be kept to a lower temperature for the samples treated with thermal annealing routes, as the *ex-situ* thermal annealing results provided in **Figure** S3c.

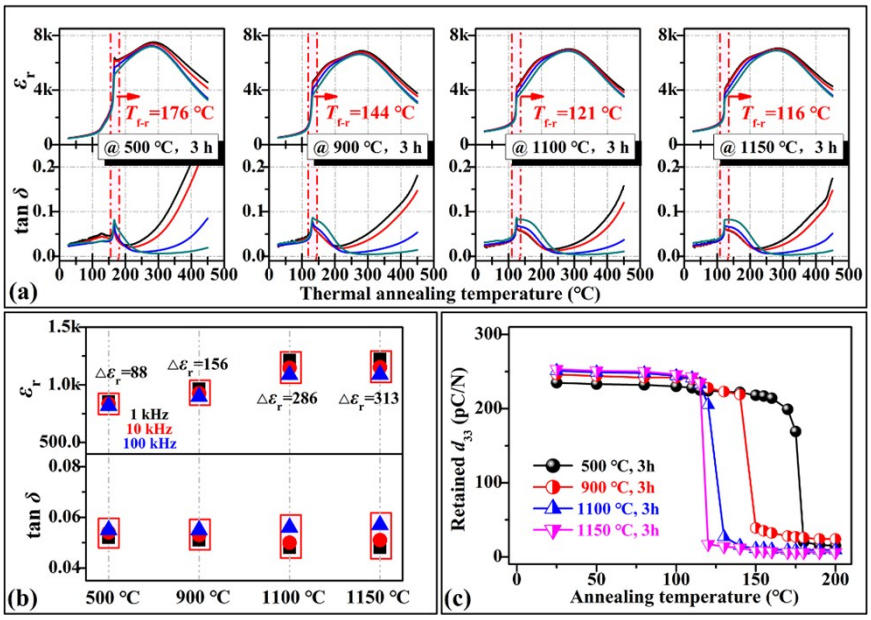

Figure S3. (a) Temperature-dependent relative dielectric permittivity (ε_r) and loss tangent (tan δ) of the LNQ1100 samples thermal annealed in nitrogen atmosphere at

different temperatures (500 ℃, 900 ℃, 1100 ℃ and 1150 ℃), and the frequency of 100, 1k, 10k and 100kHz were used to detect the dielectric signal. (b) The frequency-dependent (1 kHz, 10 kHz and 100 kHz) variations of relative permittivity ε_r and loss tangent tan δ derived from the samples thermal annealed at different temperatures. (c) Temperature-dependent variations of the small signal piezoelectric strain coefficient d_{33} measured in an *ex-situ* way.

3.2 XPS spectrum

Figure S4 gives the high-resolution XPS results for samples treated with six different routes. **Figure** S4a gives the XPS spectrum of Bi4f, and **Figure** S4b gives the XPS spectrum of Ti2p3. From the obvious discrepancy of Bi4f spectrum and the similar Ti2p3 spectrum, it can be inferred that the quenching treatment may greatly affect the element distribution of the A-site rather than the Ti-site. As the thermal annealing treatment in nitrogen atmosphere provided in **Figures** S3 and S4, quenching effects on T_d, d_{33} and O1s circumstance can be fully recovered at high temperatures, further indicating that the circumstance evolution of two oxygen states is the thermodynamic result of the A-site element redistribution

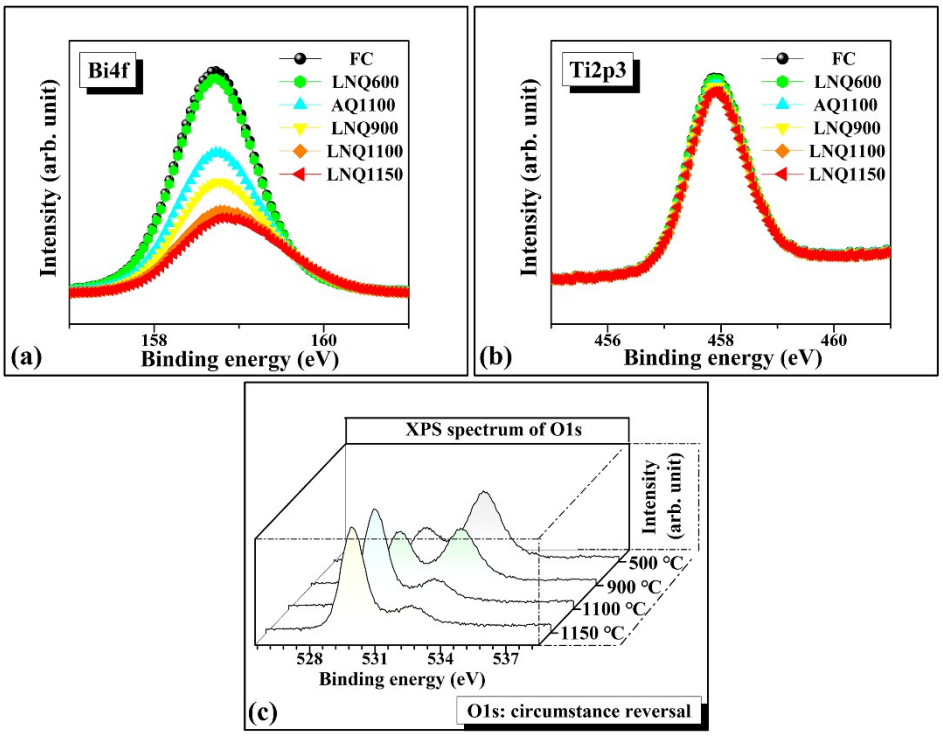

Figure S4. High resolution XPS spectrum of (a) Bi4f and (b) Ti2p3 for six different

heat treatments measured at room temperature. (c) High resolution XPS spectrum of O1s for the LNQ1100 samples thermal annealed in nitrogen atmosphere at different temperatures (500 ℃, 900 ℃, 1100 ℃ and 1150 ℃) measured at room temperature.

3.3 Electro-strain and ferroelectric behaviors

3.3.1 Temperature-dependent electro-strain and ferroelectric behaviors

For an intuitive comparison, three representative temperatures (25 ℃, 100 ℃ and 150 ℃) are selected to show the temperature-dependent ferroelectric and piezoelectric properties variations, as provided in **Figure S5**. The pinched *P*-*E* loops and disappeared negative electro-strain indicate that the samples with FC and AQ1100 treatments tend to depolarize near 100 ℃ and 150 ℃, consistent with previous reports. [2-4] From 25 to 150 ℃, although accompanied with the thinner *P*-*E* loops and decreased negative electro-strain, the well-shaped ferroelectric *P*–*E* loops and the normal butterfly-like *S*-*E* curves still confirm the ferroelectric nature. [2-4]

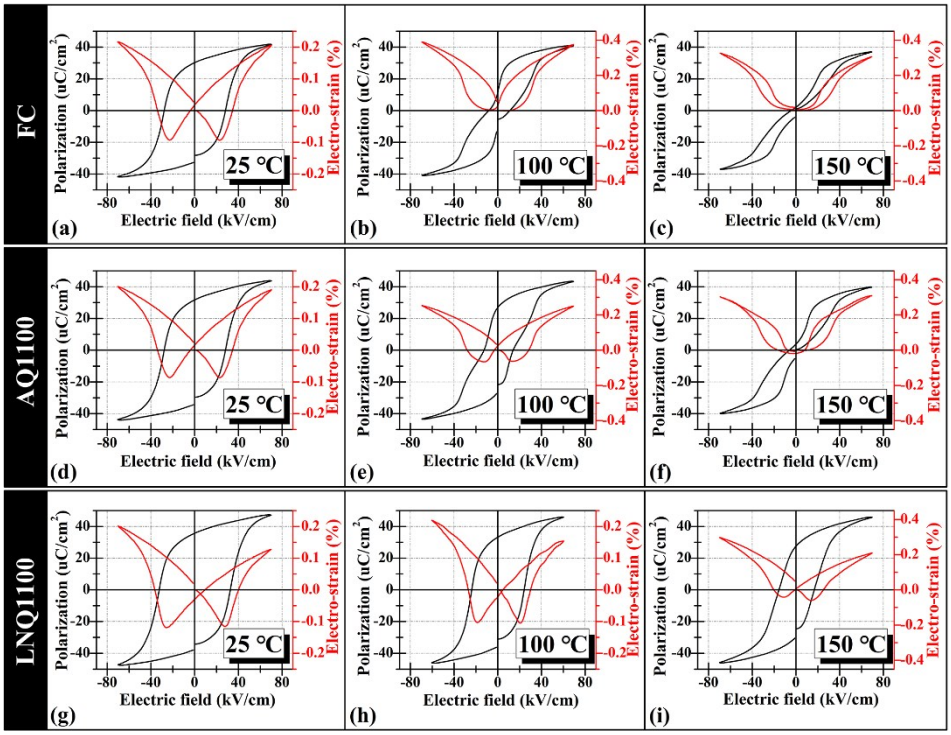

Figure S5. Temperature-dependent ferroelectric and electro-strain variations of the samples treated by (a, b, c) FC, (d, e, f) AQ1100 and (g, h, i) LNQ1100 methods. The space prevents too many temperatures here, so the representative 3 temperatures (25 ℃, 100 ℃ and 150 ℃) are selected.

3.3.2 Frequency- and *E*-field-dependent electro-strain and ferroelectric behaviors

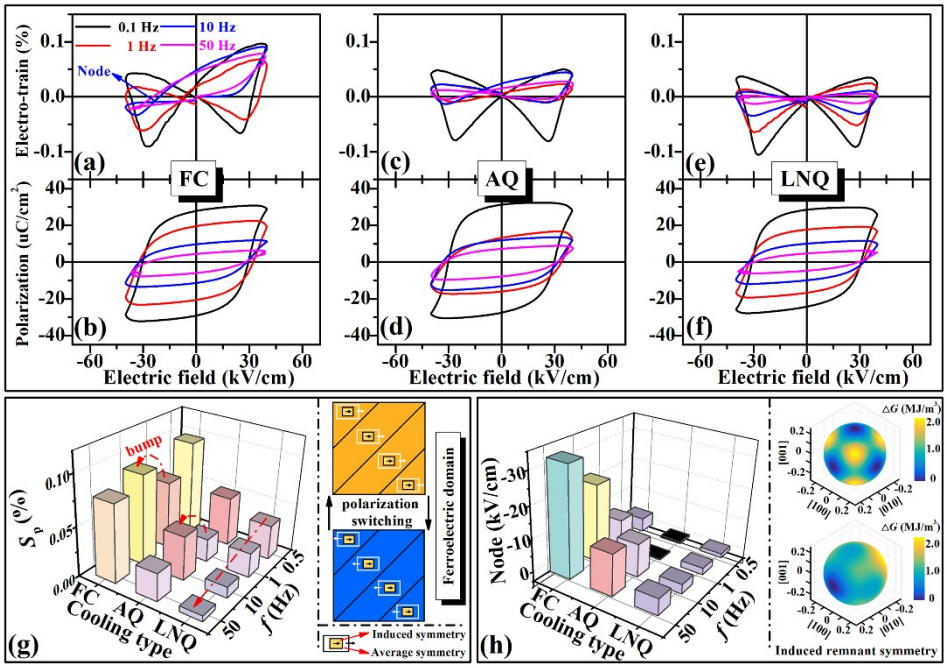

Figure S6. Frequency-dependent (0.1 Hz, 1 Hz, 10 Hz and 50 Hz) electro-strain and ferroelectric variations of the poled samples (after 90 days aging) treated by (a, b) FC, (c, d) AQ1100 and (e, f) LNQ1100 methods. The noun "node" is utilized to describe the cross-point of the butterfly-like *S*-*E* curves. (g) Intuitionistic histogram utilized to show the variation of positive electro-strain (S_{pol}) against different cooling types and different frequencies. The models shown in the right part are utilized to illustrate the relaxor response of ferroelectric domains to the *E*-field from the conceptual perspective of the ferroelectric domains. (h) Intuitionistic histogram utilized to show the variation of remnant polarization (P_r) against different cooling types and different frequencies. The models shown in the right part are utilized to illustrate the relaxor response of ferroelectric domains to the *E*-field from phenomenological perspective of free-energy.

Defect dipoles and the spontaneous dipoles require different time to response to the external loading *E*-field. Therefore, the defect chemistry can be reflected from the frequency-dependent electro-strain and ferroelectric measurements. [5,6] It is recognized that the more defects in the perovskite lattice, the greater the asymmetry after the aging treatment for the poled samples will be shown on the *S*-*E* and *P*-*E* loops, and the degree

of the asymmetry will be increased with the increasing frequency. [7,8] According to the XPS spectrum of O1s provided in the main text (**Figure** 2e), we can see that quenching treatment will lead to the circumstance reversal of oxygens. If the circumstance reversal comes from the vastly increased oxygen vacancies, the corresponding increased defect dipoles will lead to the more asymmetrical *S*-*E* and *P*-*E* loops. However, the experimental results are opposite to our assumptions, as provided in **Figures** S6a-S6f. According to the results shown in the main text, we think that the heterogeneous distribution of A-site elements by quenching treatment is supposed to contribute to the circumstance reversal of two oxygen states. And, the heterogeneous distribution of A-site elements leads to the increased coherence length of ferroelectric lattice, yielding to a stiffer ferroelectric domain behavior. The asymmetric and frequency-dependent *S*-*E* and *P*-*E* loops can thus be expected in the samples with shorter ferroelectric order, which should be attributed to the remnant effects of *E*-field, or more precisely, the relaxor responses of ferroelectric domains to the *E*-field.

Figure S7a-S7f shows the *E*-field-dependent electro-strain and ferroelectric variations of the samples treated by FC, AQ1100 and LNQ1100 methods. From the histograms provided in S7g and S7h, one can see that quenching slightly increases the coercive *E*-field (E_C) and remnant polarization (P_r).

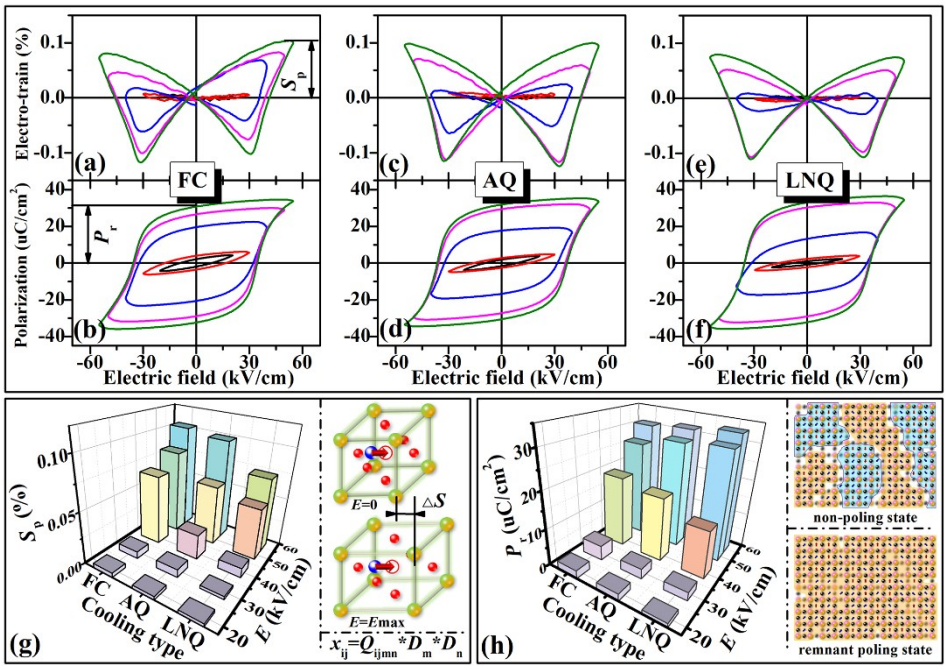

Figure S7. Electric-field-dependent (20, 30, 40, 50 and 60 kV/cm) electro-strain and ferroelectric variations of the samples treated by (a, b) FC, (c, d) AQ1100 and (e, f) LNQ1100 methods. (g) Intuitionistic histogram utilized to show the variation of positive electro-strain (S_{pol}) against different cooling types and different E-fields. (h) Intuitionistic histogram utilized to show the variation of remnant polarization (P_r) against different cooling types and different E-fields.

3.4 Detailed typical butterfly amplitude and phase hysteresis loops

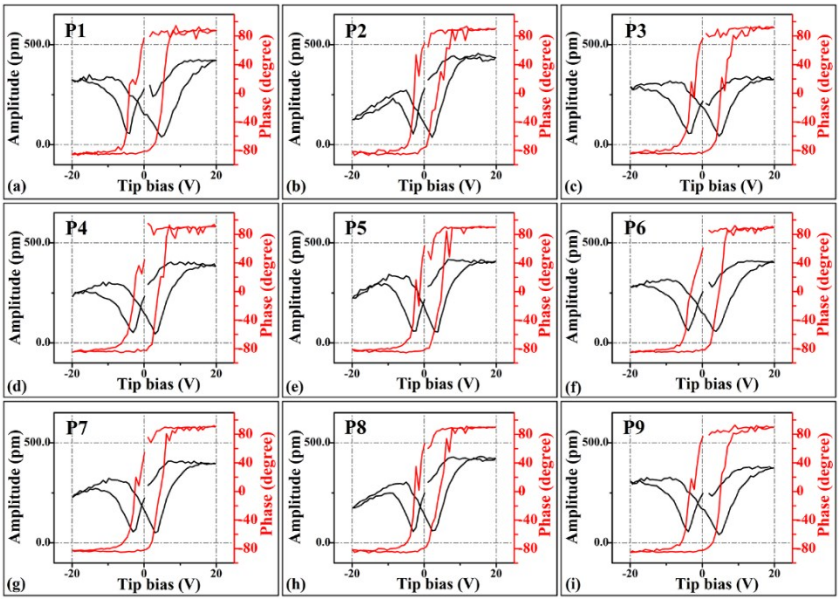

Figure S8. Typical butterfly amplitude loops and phase hysteresis loops measured at local dots (-20 V ≤ the swept voltage ≤ 20 V), where the data of (a-i) are derived from the samples treated by the FC method.

To better show the discrepancies of local piezo-responses, switching-spectroscopy PFM (SSPFM) is applied to analyze the local piezoelectric properties. Measured at local positions (ten positions for each sample, and the representative one can be seen in the main text) on the domains, three representative butterfly amplitude and phase hysteresis loops (**Figures S8, S9** and **S10**) are selected to show the discrepancies of local piezo-responses. Obvious discrepancies can be observed between the non-quenching (FC) and quenching samples (AQ1100 and LNQ1100), while slight discrepancies can be observed for the samples treated with different quenching routes (AQ1100 and

LNQ1100). As the expanded amplitude and phase hysteresis loops generally reflected in **Figures S8, S9** and **S10**, one can conclude that it would be harder for the domains to rotate after the quenching treatment.

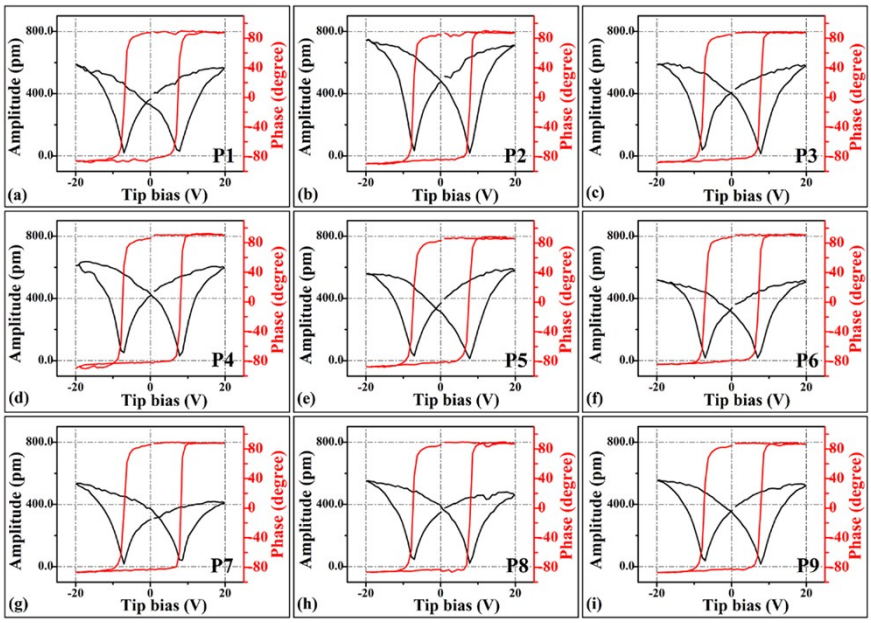

Figure S9. Typical butterfly amplitude loops and phase hysteresis loops measured at local dots (-20 V ≤ the swept voltage ≤ 20 V), where the data of (a-i) are derived from the samples treated by the AQ1100 method.

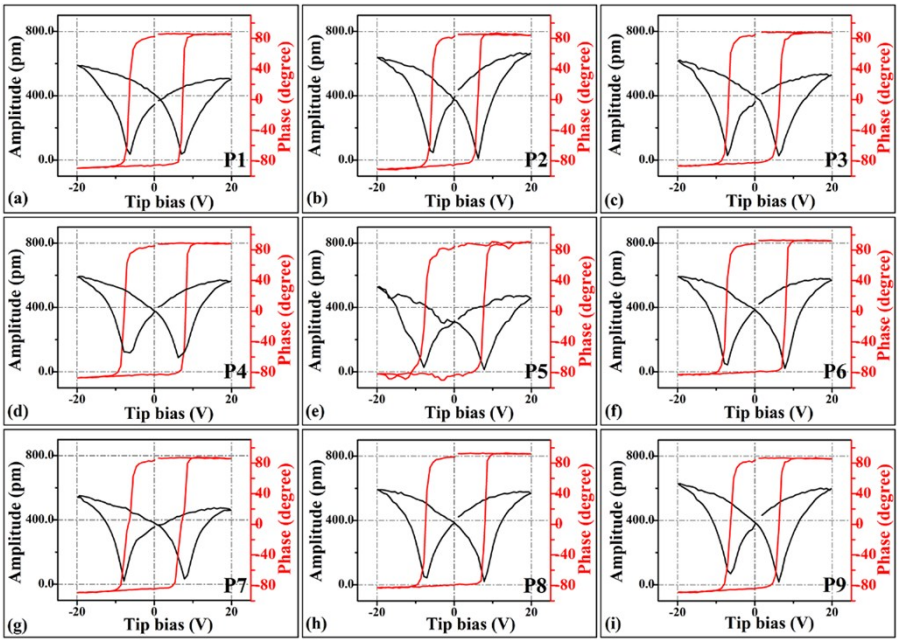

Figure S10. Typical butterfly amplitude loops and phase hysteresis loops measured at local dots (-20 V ≤ the swept voltage ≤ 20 V), where the data of (a-i) are derived from the samples treated by the LNQ1150 method.

3.5 Low-resolution XRD results

Low-resolution XRD patterns of unpoled samples treated with different quenching methods are provided in **Figure** S11. All samples possess a typical perovskite phase, indicating that the average structure of this homogeneous solid solution has not been affected by quenching treatment. Compared with the XRD patterns of the samples treated with FC and LNQ600, clear (110), (111), (200), (211), (220) peaks broadening and splitting can be observed for the samples treated with AQ1100, LNQ900, LNQ1100 and LNQ1150 routes. This observation can, in fact, be interpreted as the increased coherence length of the ferroelectric ordering. The high-resolution XRD results and the corresponding Rietveld fitted analysis can be seen in our main text (**Figures** 3d-3f).

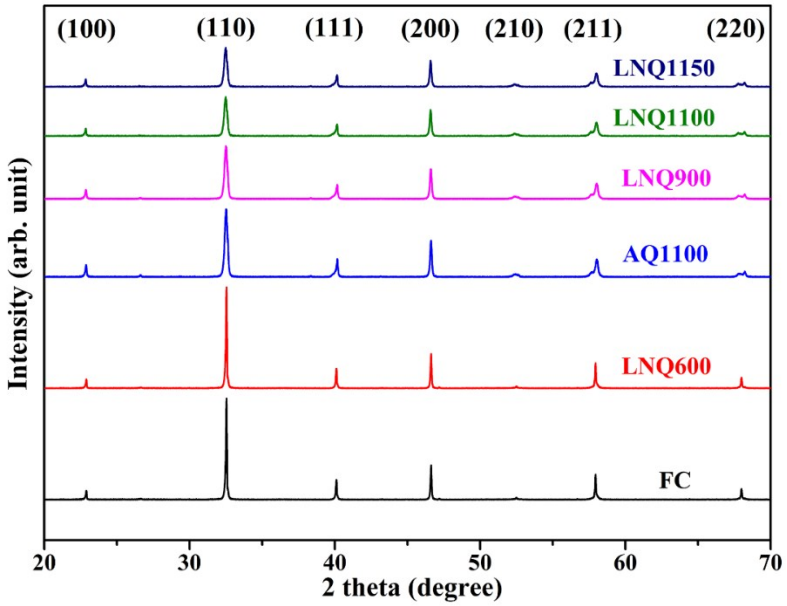

Figure S11. Average phase structure part: Normal XRD patterns of the samples treated with FC, LNQ600, AQ1100, LNQ900, LNQ1100 and LNQ1150 methods.

References

[1] Y. L. Li, L. E. Cross, L. Q. Chen, *J. Appl. Phys.* 2005, ***98***, 064101.

[2] S. T. Zhang, A. B. Kounga, E. Aulbach, Y. Deng, *J. Am. Ceram. Soc.* 2008, ***91***,

3950–3954.

[3] G. Viola, R. McKinnon, V. Koval, A. Adomkevicius, S. Dunn, H. Yan, *J. Phys. Chem. C* 2014, ***118***, 8564–8570.

[4] J. Zhang, Z. Pan, F. F. Guo, W. C. Liu, H. Ning, Y. B. Chen, M. H. Lu, B. Yang, J. Chen, S. T. Zhang, X. Xing, J. Rödel, W. Cao, Y. F. Chen, *Nat. Commun.* **2015**, *6*, 6615

[5] Z. T. Li, H. Liu, H. C. Thong, Z. Xu, M. H. Zhang, J. Yin, J. F. Li, K. Wang, J. Chen, *Adv. Electron. Mater.* **2019**, *5*, 1800756.

[6] W. Hu, Y. Liu, R. L. Withers, T. J. Frankcombe, L. Norén, A. Snashall, M. Kitchin, P. Smith, B. Gong, H. Chen, J. Schiemer, F. Brink, J. W. Leung, *Nat. Mater.* **2013**, *12*, 821.

[7] T. Granzow, E. Suvaci, H. Kungl, M.J. Hoffmann, *Appl. Phys. Lett.* **2006**, *89*, 262908.

[8] J. Lv, X. Lou and J. Wu, (2016). *J. Mater. Chem. C* **2016**, *4*, 6140-6151.